# Interpretation of temperature distribution observed on W-ITER-like PFUs in WEST monitored with a very-high-resolution IR system

A Grosjean, M H Aumeunier, Y Corre, M Firdaouss, J Gaspar, J Gerardin, J P Gunn, X Courtois, R Dejarnac, M Diez, et al.

HAL Id: hal-03578445

https://amu.hal.science/hal-03578445

Submitted on 17 Feb 2022

# Interpretation of temperature distribution observed on W-ITER-like PFUs in WEST monitored with a very-high-resolution IR system

A. Grosjean[1+], M.H. Aumeunier[1], Y. Corre[1], M. Firdaouss[1], J. Gaspar[2], J. Gerardin[3], J. P. Gunn[1], X. Courtois[1], R. Dejarnac[3], M. Diez[1], L. Dubus[1], M. Houry[1], C. Pocheau[1], E. Tsitrone[1] and the WEST team*

[1]*CEA, Institute for Research on Fusion by Magnetic confinement, 13108 Saint-Paul-Lez-Durance, France*
[2]*Aix Marseille Univ, CNRS, IUSTI, Marseille, France*
[3]*Institute of Plasma Physics, Czech Academy of Sciences, 182 00 Prague, Czech Republic*

*\* See http://west.cea.fr/WESTteam*

[+]*E-mail address of the first author: alex.grosjean@cea.fr*

During the 2019 experimental campaign, the WEST tokamak was partially equipped with ITER-like plasma facing units (PFUs) made of discrete monoblocks (MBs) in one of the twelve lower divertor sectors. The magnetic field lines can enter the gaps between two MBs and strike their leading edges (LEs) with near normal incidence, leading to high localized heat flux, temperature and thermomechanical stress during both stead-state operation and transients. Exposed leading edges are a particular matter of concern because of potential crack formation, recrystallization or even melting of tungsten. During the 2019 experimental campaign in WEST, five of them were misaligned (vertical misalignment h = 0.30 ± 0.1 mm) with their poloidal leading edges exposed to the plasma heat flux. A medium wavelength IR filter (MWIR: 3.9 ± 0.1 μm) was installed in the very high resolution infrared system, featuring a submillimeter spatial resolution (~0.1mm/pixel). This system has a temperature detection threshold of $T_{threshold, BB} \approx 250°C$. In this paper, thermal analysis will be presented with a specific focus on overheating of poloidal and toroidal edges using post-mortem measured emissivity maps. The study reveals an unexpected hot spot in the top LE corner of misaligned PFUs at the outer strike point (OSP). Photonic calculations were performed with different emissivity on top and lateral surfaces, in order to consider the complex reflectance characteristics in the toroidal gaps. During this experiment, the Larmor radius (0.35 mm) is comparable to the gap size. Thus, the helical trajectory of the particles may significantly affect the heat load distribution in the edges vicinity. Heat load simulations were performed with ion orbit modeling that consider the Larmor radius, to study its impact on the thermal distribution of the MB. The photonic simulations showed that it was possible to observe a false hot spot at the top LE corner, with both optical approximation (OA) and ion orbit (IO) modeling, due to reflections and different emissivity values.

## 1. Introduction

One of the aims of the WEST tokamak is to test ITER Plasma-facing units (PFUs) prototypes. In this context, water-cooled PFU prototypes consisting of tungsten (W) monoblocks (MBs) bonded to CuCrZr cooling tubes were installed in the test divertor sector [1]. These PFUs are designed to extract the high power coming from the plasma [2]. The subdivision of plasma-facing units (PFUs) into discrete MBs with no specific shaping (see left panel of Figure 1), means that the magnetic field lines (MFLs) can enter the gaps between them and strike their sides. In the toroidal gaps, the MFLs strike the toroidal surface of the MB with a shallow angle ($\theta_{//} \sim 1 - 2°$), while the MFLs, in the poloidal gaps, strike the poloidal surface with near-normal incidence ($\alpha + \pi/2$), leading to higher localized heat fluxes. This effect is enhanced by possible misalignments between MBs [3] (see right panel of Figure 1). The

WEST divertor is designed such that the plasma flowing along the magnetic field lines impacts the MB top surfaces at glancing angles (α ~ 2.5° in the shot presented in this study: #54934) [4]).
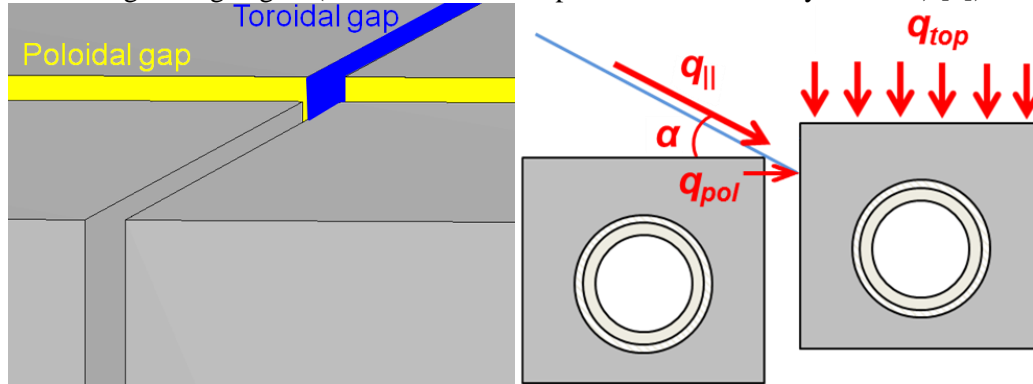


Figure 1 Left panel: poloidal gaps (yellow) between two PFUs, and toroidal gaps (blue) between two monoblocks of the same PFU. Right panel: magnetic field line impinging the poloidal side of the misaligned monoblock (blue line) with a parallel heat flux coming from the scrape-off layer ($q_{//}$) and an incidence angle (α). Heat flux absorbed on the top surface ($q_{top}$), and on the side surface ($q_{pol}$) are also depicted on the misaligned MB. In case of misalignment, the exposed area is larger on the poloidal side.

The simplest approach to quantify the incident heat flux is the optical approximation (OA) which is the geometric projection of the parallel heat flux onto the PFU surfaces. Each plasma particle, ion or electron, is supposed to strictly follow the magnetic field line (MFL), gyro-radius and sheath effects are neglected. The OA is also known as the guiding center approximation. The projection of the MFL onto the plane parallel to the toroidal face makes an angle $\theta_\perp$ with the top surface (see right panel of Figure 2). The projection of the MFL onto the top surface makes an angle $\theta_\parallel$ with the toroidal surface (see left panel of Figure 2). This angle arises because the magnetic flux surfaces are tilted with respect to toroidal surface of the MB.
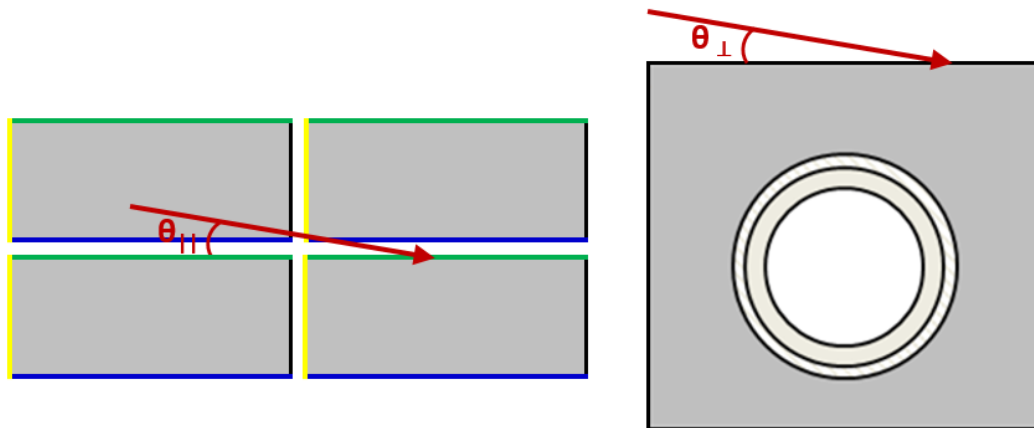


Figure 2 Left panel: View from top of the projection of the MFL onto the top surface that makes an angle $\theta_\parallel$, with the toroidal surface of the MB. In the top view, the different edges discussed in this paper are represented: the toroidal edges in high field side (HFS) and low field side (LFS) are represented in green and blue respectively, while poloidal leading edges are represented in yellow. View from cooling tube axis of the projection of the MFL onto the toroidal surface that makes an angle $\theta_\perp$, with the top surface of the MB.

The incident heat flux to the surfaces is related to $\theta_\perp$ and $\theta_\parallel$ and can be expressed with the incidence angle α between the magnetic field vector and the different surfaces of the MB: top, poloidal and toroidal surfaces through:

$$q_{top} = q_{\parallel}(\vec{B}.\vec{n}_{top}) = q_{\parallel}\frac{B_p}{B} \approx q_{\parallel}\sin\theta_{\perp} \approx q_{\parallel}\sin\alpha \qquad (1)$$

$$q_{tor} = q_{\parallel}(\vec{B}.\vec{n}_{tor}) = q_{\parallel}\frac{B_R}{B} \approx q_{\parallel}\sin\theta_{\parallel} \qquad (2)$$

$$q_{pol} = q_{\parallel}(\vec{B}.\vec{n}_{pol}) = q_{\parallel}\frac{B_T}{B} \approx q_{\parallel}\sin(\alpha+\beta) \qquad (3)$$

With $\vec{B} = (\vec{B}_R, \vec{B}_T, \vec{B}_P)$ respectively the radial, toroidal and poloidal component of the total magnetic field and β being the angle between the top surface and poloidal-side surface (90° for a sharp edge and 45° for a 1x1 mm chamfer edge). Since in tokamaks $B_T \gg B_P$, the total B-field usually reaches the targets with very shallow angles on the top surface (0.5 to 2.5° in WEST). Shallow angles are also expected at the toroidal surfaces as $B_T \gg B_R$: ($\theta_{\parallel} \sim$ 1-2° in WEST). With the OA, similar heat flux magnitudes are expected on top and toroidal surfaces with shallow angles. The most critical surfaces are the poloidal sides as they intercept MFLs with near normal incidence angles with no shaping, thus the full parallel heat flux is expected on these poloidal surfaces.

The first study on actively cooled PFUs was performed with the toroidal pump limiter (TPL) of Tore Supra. The TPL was made of carbon fiber composite (CFC) tiles with a flat top surface and 2 mm rounded edges, including poloidal and toroidal gaps [5]. A series of experiments [6] was conducted in the COMPASS tokamak with a specially designed graphite inner wall limiter (IWL). In JET, running with an ITER-like wall, a sharp edge [7] and a protruding [8] W lamella (15° slope), were exposed to L-mode [9] and H-mode [10] plasmas. On ASDEX-Upgrade, an extensive series of experiments in H-mode were performed on misaligned and 15° sloped tiles using its Divertor Manipulator II system (DIM-II) up to 1.1 mm to observe tungsten melt motion [11]. TEXTOR also ran experiments on tungsten melt motion with castellated W plates (2mm thick) exposed up to 3cm (LCFS) [12]. Tungsten blocks with 0.3 and 1 mm misalignments were exposed in DIII-D Helium plasmas [13]. The KSTAR device exposed some W blocks with misalignment from 0.3 mm up to 2 mm [14]. Magnum PSI and PILOT-PSI respectively ran an extensive set of linear plasmas with grazing angles (4 - 7°) on misaligned W blocks to replicate L-mode and H-mode tokamak divertor-like regimes [15], [16]. Experimental studies on leading edges through IR thermography have already been thoroughly performed on several devices, with different magnetic equilibria such as limiter or divertor configuration, or on linear devices, with different components, materials, and geometries, but never on a real, actively cooled ITER-like W PFU prototype, with a high spatial resolution of the IR monitoring system as performed in WEST [17].

## 2. Experimental configuration

A first experimental campaign (C3) was performed in WEST in 2018 with high PFU misalignment, up to 0.8 mm and limited RF heating power (up to 6 MW). 900°C maximum temperature was measured by the very-high-resolution (VHR) infrared imaging system with a parallel heat flux of about 45 MW.m$^{-2}$ [17]. For these conditions, thermal modeling predicts that the leading edges of the misaligned PFUs cannot withstand the 200 MW.m$^{-2}$ parallel heat flux that is required to reach ITER-relevant power loads of 10 MW.m$^{-2}$ on the top flat surface as foreseen in the WEST project. In addition, a visual inspection performed after this experimental campaign revealed crack networks and partial melting on the overexposed leading edges presumably linked to a combination of steady state and transient loads like disruptions [18]. For both reasons, it was decided to realign all the PFUs meeting the ± 0.3 mm tolerance for the following experimental campaign in 2019 (C4) performed with higher RF heating power (up to 9 MW). Regarding the IR settings, during the C3 experimental campaign, a small wavelength infrared (SWIR) filter was used (give the wavelengths explicitly), and that implies a high temperature threshold that limited the studies to the hot leading edges only, over a toroidal extension of X mm. it was decided to use a MWIR filter to lower the temperature detection threshold in order to be able to study the thermal scene over a full MB length with moderate heat flux as achieved in WEST during the C3 experimental campaign [4]. As a result, the VHR temperature database was considerably

extended. VHR IR data were successfully taken on poloidal and toroidal LEs, on both outer strike point (OSP) and inner strike point (ISP) regions. At the same time, recent measurements on realistic tungsten samples showed that the MWIR filter is more sensitive to emissivity variations [19]. The emissivity was measured after the C4 experimental campaign in the range from 0.06 in the strike point (SP) areas up to 0.8 in cold redeposition areas, using the method developed for in-situ emissivity measurements developed in [20]. First experimental results highlighted unexpected phenomena such as a temperature drop close to the LE attributed to an emissivity drop. A new calculation was performed with non-uniform emissivity in the toroidal direction. An unexpected hot spot also appeared in the top LE corner of a misaligned PFU. This phenomenon is not predicted by the optical approximation (OA), commonly used for engineering design of PFCs and diagnostics. For a series of shots monitored with the VHR IR system , the electron temperature was measured with the divertor flush-mounted Langmuir probes ($T_e$ = 40 eV) [21], leading to an ion Larmor radius of 0.35 mm, which is close to the poloidal and toroidal gap size (0.5 mm), located at this specific area. The ion orbit (IO) modeling predicts a heat flux enhancement at this specific location due to the ion Larmor effects [3]. On top of that, the thermal-radiative properties of tungsten may affect the IR measurements. This paper proposes to investigate the origins of these unexpected phenomena on poloidal and toroidal edges.

The VHR IR system that monitors the test divertor sector is presented in section 2. IR data and post-mortem emissivity measurements are shown for two ITER-like PFUs located in the high heat flux area. The emissivity distribution measured during post-mortem measurements is used in section 3 to analyze the temperature drop observed in the IR data.  Section 4 shows the heat load and temperature distribution, with a specific focus on the hot spot observed on the top LE corner. The heat flux distribution is computed separately with OA (4.1) and IO (4.2) modeling. Photonic simulations are performed including optical blurring effects of the optical system, an isotropic emissivity with different values for top, poloidal and toroidal surfaces, and complex reflectance model to help interpret the IR data. A discussion is proposed as a conclusion on the impact of thermal-radiative properties on IR measurements and contributions of the ion Larmor radius effect in the temperature distribution observed with the VHR IR data, with a specific focus at the top LE corner.

The WEST lower divertor has 12 sectors each equipped with 38 PFUs. During the C1-C4 experimental campaigns achieved in 2017-2019, most of these PFUs were made of uncooled W-coated graphite components. During the C4 (2019) experimental campaign, one sector, called the "test divertor sector", was equipped with a set of 14 ITER-like PFU prototypes [22] (see left panel of Figure 3), each composed of 35 tungsten monoblocks (MBs) separated toroidally by 0.5 mm gaps (see Figure 1). Among them, 4 have sharp LEs and 10 have a 1x1 mm 45° chamfer on both leading and trailing edges. The PFUs were tested in WEST under plasma discharges heated by two lower hybrid (LH) antennas with injected power up to ~5 MW [23]. The ITER-like PFUs were monitored by a very high-resolution (VHR) infra-red camera (see right panel of Figure 3) in the middle wavelength IR (MWIR) band: λ = 3.9 ± 0.1 μm during C4 experimental campaign [24].
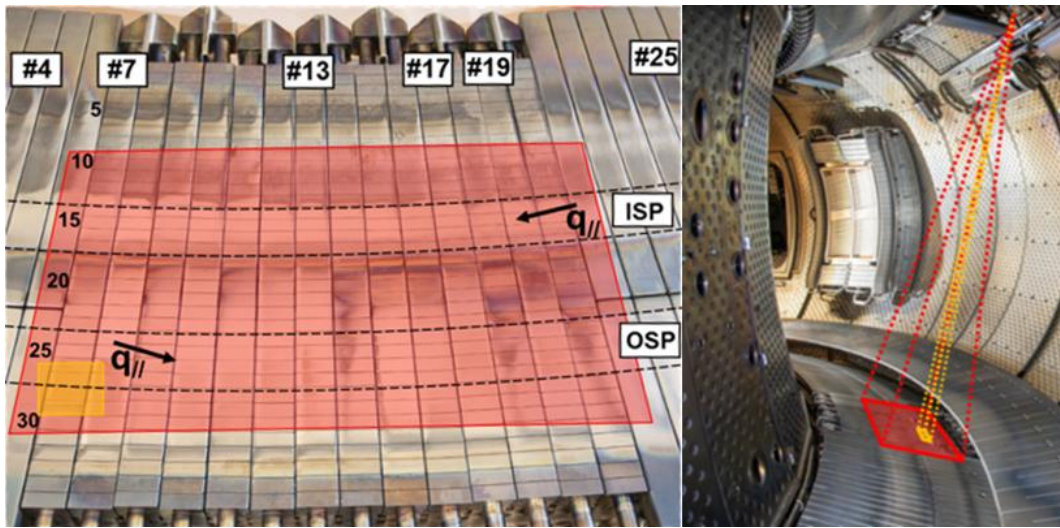
Figure 3 Left panel: focus on the 14 ITER-like PFUs of the WEST test divertor sector. PFUs monitored by the VHR IR camera are shown in the red areas from PFU #6 to PFU #21. Orange area represents the field of view (FoV) monitored by the VHR IR camera on PFU #7 and #8, discussed in this work. MBs are labeled from MB1, high field side (HFS), to MB35, low field side (LFS), as indicated in the PFU #6. Black arrows indicate the parallel heat flux direction in inner (HFS) and outer (LFS) divertor. Right panel: tangential view of the WEST vacuum vessel showing the VHR IR FoV (orange) and the potential position that can be observed with the VHR (red).

The shot #54934 studied here was performed during the dedicated experiments on the LE described in[4]. During the experiments, a ~4 MW flattop injected LH power was performed during 6s, to reach the thermal equilibrium of the PFU in order to simplify the thermal modeling required for the parallel heat flux analysis performed in [4].
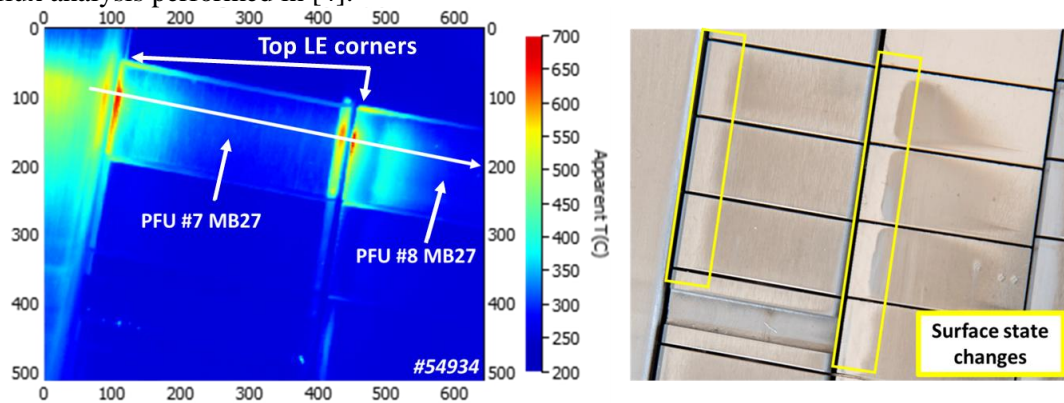


Figure 4 Left panel: IR thermography on shot #54934 monitoring PFU#7 (chamfered) and #8 (sharp) at the OSP (MB27). Right panel: picture of the same FoV taken after the C4 experimental campaign that evidences the surface states changes. The FoV shows a top view of the WEST divertor, whose PFUs run along the poloidal direction.

The IR data presented in the left panel of Figure 4, are interesting and complex. In this FoV, the PFU #7 and #8 have chamfered and sharp edges, with 0.28 mm and 0.40 mm vertical misalignments at the MB27, respectively. The black-body temperature, also called the apparent temperature, is the temperature seen by the infrared system, collecting the photons in its detector. The submillimeter spatial resolution of the VHR IR system (~0.1 mm/pixel), permits here to perform a detailed study of the leading-edge effects for both geometries. In this analysis, the black-body temperature is the same for sharp and chamfered LEs while modeling predicts higher temperature for the PFU #8, that have a

greater misalignment and a higher heat flux on the poloidal surface. In addition, the black-body temperature drops in the first millimeters in the toroidal location, and the top LE corners exhibit high temperatures, similar to the one measured at the poloidal LE. Neither phenomena are predicted by thermal modeling based on the OA. Unexpected phenomena can be attributed to significant surface state changes at the top surface of the MB (see right panel of Figure 4) that affect the thermal-radiative properties of tungsten, inducing an inhomogeneous distribution of the emissivity in both poloidal and toroidal directions. A specific study was performed on a MB located at the OSP with optical microscopy, at the LE (left panel of Figure 5) and at the top LE corner (right panel of Figure 5).
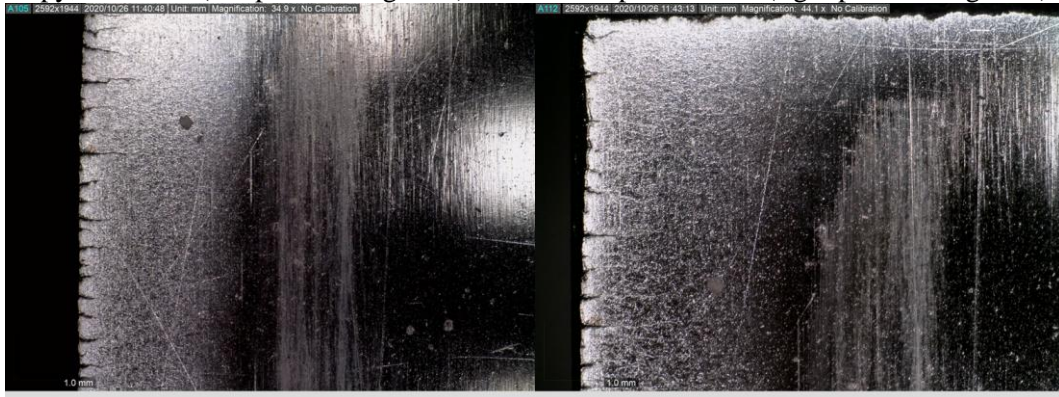


Figure 5 Optical microscopy pictures taken on a MB located at the OSP: top-view of the MB, focusing on the LE (left panel), and the top LE corner (right panel) with a 34 and 44 magnification respectively.

For this reason, a post mortem emissivity measurement was performed on the misaligned PFUs, at low temperature ~50°C, with a 3 to 5 µm filter (instead of $3.9 \pm 0.1$ µm used in the C4 campaign), and at atmospheric pressure. The emissivity maps are shown in Figure 6 for PFUs #7 and #8. Note that the dedicated experiments on LEs were performed in the middle of the experimental campaign with a magnetic configuration that differs from the standard pulses (OSP located on MB27 instead of MB23-25) and before a two week helium campaign, which may induce differences in the surface state between the dedicated experiments and the post-mortem emissivity measurement.
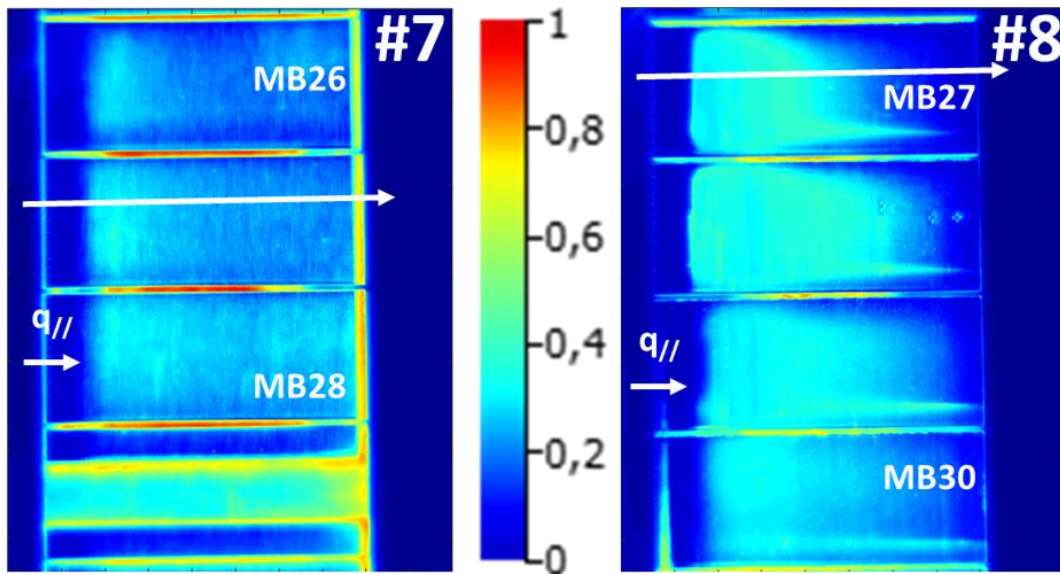


Figure 6 Emissivity measurement performed at 50°C and atmospheric pressure on ITER-like PFUs after the C4 experimental campaign at the OSP: chamfered PFU #7 (left), sharp PFU #8 (right).

The emissivity pattern is strongly correlated to the surface state changes observed in the picture of Figure 4 after the C4 experimental campaign, with a similar pattern for PFU #7 and #8. A rather constant emissivity around 0.4 far from the LE a significant drop in the first 4 mm after the LE and an increase of the emissivity value at the LE, caused by the crack network and the manufacturing of the chamfered edges (for PFU #7).

## 3. Poloidal leading edge

The emissivity increases with temperature; hence a correction of the emissivity value was required to match with experimental temperatures measured with the VHR. To take this variation into account, the emissivity value at 50°C, for a given point of the toroidal profile, was extrapolated to the corresponding temperature of this point. The extrapolation is based on emissivity measurements performed on realistic W samples [19], with weighted-average of the two closest evolution trends. This value is found by iterating between emissivity and temperature values until they converge. The corresponding (ε, T) pair was found for every pixel of the toroidal profile studied in the VHR FoV. The toroidal profiles of emissivity are shown in Figure 7. Note that the profiles do not have the same length, this is due to the limited FoV of the VHR, and the extrapolated emissivity is only measured where there is IR data.
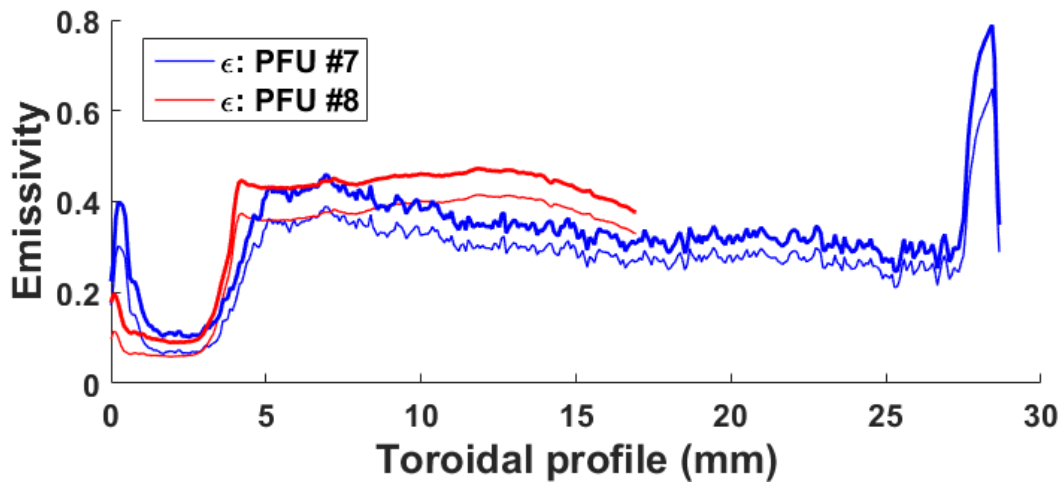


Figure 7 Toroidal profiles of emissivity, measured at 50°C (thin curves) and extrapolated to the MB temperature (thick curves) for PFU #7 (blue), #8 (red).

Measurements at 50°C clearly show that the assumption of constant emissivity is not valid, but also that the same emissivity value at the poloidal LE, for different PFUs cannot be a reasonable assumption. It also shows here what can be deduced from Figure 4, that the emissivity is higher on the chamfered LE (PFU #7), which explains why the parallel heat flux required to match the experimental data was higher at this LE for the same pulse (#54934). Several sharp gradients (at the LE , 4-5 mm and at the trailing edge) are observed in the toroidal profile. The increase of the emissivity at the LE is mainly due to the crack network observed in post mortem analysis [18] and visual inspection. The emissivity drop observed from 0 to 4-5 mm is assumed to be caused by a higher net erosion in this specific area. A hypothesis is that it may be caused by the combination of Larmor radius [25] and sheath effects [26], that locally increase the heat load over a few mm at the LE vicinity as mentioned in [4] and [27]. This toroidal pattern was observed in all misaligned PFUs measured with or without chamfer. The increase observed at the trailing edge (~30 mm) is due to the chamfer, which is a cold area shadowed from the plasma, prone to redeposition, and seen by the VHR with an inclination of the surface that are expected to enhance the emissivity [28] during the measurements (see Figure 6). In addition, it is possible to see the variation between extrapolated and measured emissivity. It varies with the temperature, but also with the measured emissivity at 50°C. The higher the measured emissivity is, the greater is the

discrepancy between extrapolated and measured emissivity. By using the extrapolated emissivity evaluated as function of the IR temperature measurement in first approximation, it is now possible to apply this non-uniform emissivity correction to the black-body temperature measured with the IR system, during the C4 experimental campaign. The toroidal profiles obtained with IR measurement can be corrected with non-uniform emissivity, which represents a significant progress compared to what was already performed in [4] with constant emissivity. An example of the non-uniform emissivity correction applied to PFU #8 is shown in Figure 8.
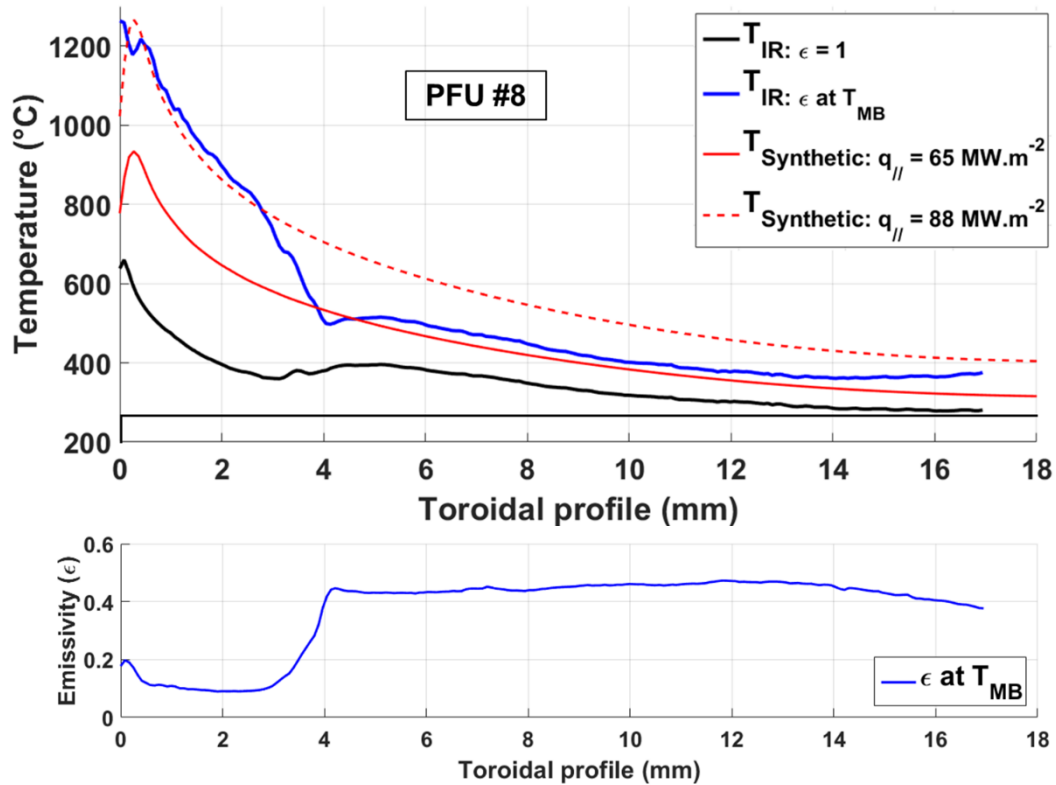


Figure 8 Top panel: Comparison between IR temperatures corrected with non-uniform emissivity (blue) with synthetic data obtained through 3D FEM modeling in a toroidal profile of PFU #8 MB27 on shot #54934. The dash-red line ($q_{//}$ = 88 MW.m$^{-2}$) matches with the IR LE temperature while the full red line (65MW.m$^{-2}$) matches with the top surface, far from the LE. The black line represents the black-body temperature. Bottom panel: emissivity extrapolated to the real temperature of the MB along the toroidal profile.

It is interesting to see that the parallel heat flux required to match with the experimental data at the poloidal LE (88 MW.m$^{-2}$), is now higher than the one that what was found for the PFU #7 (78.5 ± 9 MW.m$^{-2}$). One can also see here, that the synthetic temperature does not match the experimental temperature, corrected with emissivity extrapolated to higher temperatures. The experimental thermal decrease is not consistent, with an overestimation of the temperature at the LE potentially induced by an underestimation of the emissivity. This may reflects the limits of the study here dealing with low emissivity values. The lower is the emissivity, the higher is the discrepancy between black-body temperature and real temperature (see Figure 2 of [4]). It was shown that the emissivity could vary from shot to shot when the strike point (SP) is moved to another MB or for the Helium campaign for instance [20]. Thus the surface state during the emissivity measurement at atmospheric pressure, performed after the C4 campaign, may not be fully representative of the one of the dedicated experiments. This reinforces our idea that the emissivity must be measured inside the tokamak during dedicated experiments to process finer analyses on heat load distributions through IR thermography.

## 4. Toroidal leading edge

### 4.1. Temperature distribution based on OA modeling

During the C4 experimental campaign, in many shots monitored by the VHR IR system, it was possible to observe high temperature on the toroidal surface facing the HFS, close to the poloidal LE, equivalent to the temperature observed in the overexposed poloidal surface (~650°C black-body temperature). An example is shown in shot #54934 (see left panel of Figure 4) where the VHR monitored PFU #7 and #8, with the OSP located in the first third of MB27. The hot spot is observed at the top LE corner, a few mm away from the peak heat flux in the HFS direction (thus in the private region). Such a hot spot is not predicted by the OA model (equations (1) to (3)), as the incidence angle between the MFL and the toroidal surface ($\theta_\psi$ ~1.8°) is lower than the one with the top surface ($\alpha$ ~2.5°), meaning that the heat flux to the toroidal surface would be expected to be about 50% lower than on the top surface. A field line tracing code (PFCFlux [29]) is used to determine the wetted areas and the heat flux distribution with realistic geometry of the MB and its environment. MBs and gaps are assumed to be perfectly aligned in the toroidal direction. The wetted area on the leading edge corner is displayed in the top panel of Figure 9. On the toroidal side, the wetted area is larger near the poloidal LE (~1.5mm) than the trailing edge (~ 0.5mm). A thin band of 0.05 mm width and 1.5 mm depth is also detected on the poloidal surface because of the $\theta_{//}$ angle, as the MFLs are tilted with respect to the toroidal surface of the MB. This area receives a high heat flux ($q_{pol}$ ~ $q_{//}$) as shown in the top panel of Figure 9.
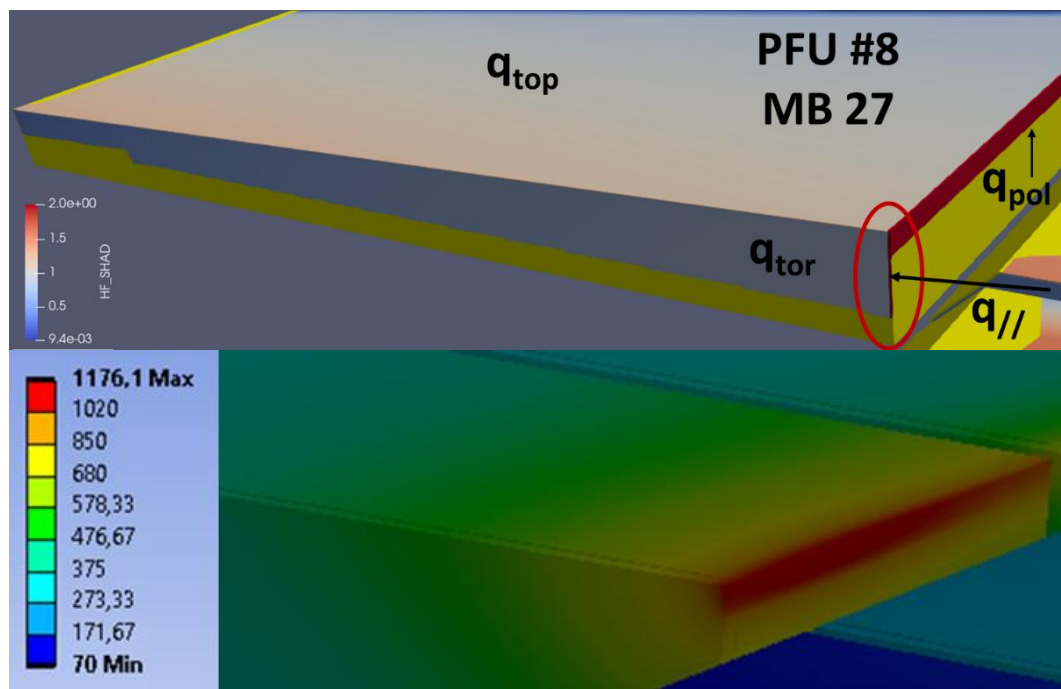


Figure 9 PFCFlux simulation based on OA modeling, shows the wetted area on the upper toroidal gap on MB27 of PFU #8 of the C4 experimental campaign. Top panel: absorbed heat flux at the top, poloidal and toroidal surfaces, with a focus on the top LE corner, and the thin poloidal band exposed, due to the toroidal gap of the previous PFU. Bottom panel: 3D FEM thermal modeling under ANSYS of PFU #8 MB7 with SOL width parameters estimated through FBG measurements (71MW.m⁻², $\lambda_q$ = 18 mm and S = 5 mm), the incidence angle and the wetted area calculated with PFCFlux, for top, poloidal, and toroidal surfaces.

The 3D FEM modeling was performed with SOL heat flux parameters based on FBG measurements ($q_{//}$ = 71MW.m⁻², $\lambda_q$ = 18 mm and S = 5 mm), applied at the top, poloidal, and toroidal surfaces. The heat flux is applied on a thin poloidal surface and toroidal surface as predicted by field line tracing codes

(PFCFlux simulation), to see if there is any notable difference in the temperature distribution around the top LE corner. Results show a slight temperature increase around the LE of about 10°C (see bottom panel of Figure 9) but nothing comparable to what is observed in the IR data having larger spatial extension (few mm away from the poloidal leading edge). The impact of thermal-radiative properties of tungsten on IR measurements can be studied with Monte Carlo Ray Tracing (MCRT) code able to reproduce realistic IR images: ANSYS-SPEOS[30]. ANSYS-SPEOS considers the modeling of observed thermal scene (3D temperature map), the photon-wall interaction, and the camera [31]. The thermal scene, used as input of photonic simulations, is the resulting temperature field computed by FEM method shown in Figure 9. The modeling of the VHR IR FoV includes the optical blurring effects, modeled with a Gaussian function ($\sigma$ = 1.2 pixels width). The optical materials properties are also considered. They include an emission model and a reflectance model which describes how the photons are emitted and reflected as a function of the wavelength, viewer's angle, and incident angle. This analysis is divided in three steps. Firstly, the impact of the optical blurring of the VHR of the camera in black body temperature is assessed (top left panel of Figure 10). Secondly, the isotropic emissivity, spatially uniform, at the top surface, at the poloidal, and the toroidal surfaces, based on averaged values obtained with the post-mortem emissivity measurement after C4 campaign are modeled (top right panel of Figure 10). The third step considers a complex reflectance model, which is a mix of diffusive (for rough surfaces) and specular (for polished surfaces) reflectance, with the emissivity assumed to be fully Lambertian here (N-power = 1) to see the impact of reflection in the VHR IR data (see bottom panel of Figure 10). The different parameters used in the ANSYS-SPEOS simulations are listed in the Table 1.

|  | Surface | Emissivity | N-power | BRDF |
|---|---|---|---|---|
| PFU #6 | Top | 0.15 | 1 | 40% diffuse |
|  | Polo | 0.15 | 1 | 40% diffuse |
| PFU #7 | Top | 0.10 | 1 | 30% diffuse |
|  | Toro | 0.20 | 1 | 60% diffuse |
|  | Polo | 0.20 | 1 | 60% diffuse |
| PFU #8 | Top | 0.10 | 1 | 5% diffuse |
|  | Toro | 0.30 | 1 | 20% diffuse |
|  | Polo | 0.20 | 1 | 20% diffuse |

Table 1 Summary of the thermal-radiative properties inputs used in the ANSYS-SPEOS simulations.

These values are qualitative, and based on visual inspection for the bidirectional reflectance distribution function (BRDF) and emissivity measurements at 50°C for the emissivity. Note that the 0.1 emissivity at the top surface was chosen to match with the reduced emissivity values measured close to the top LE corner, which is thus, not representative of the full top surface. Implementing inhomogeneous emissivity to a surface is possible but requires larger development, not necessary for the qualitative analysis presented in this paper.
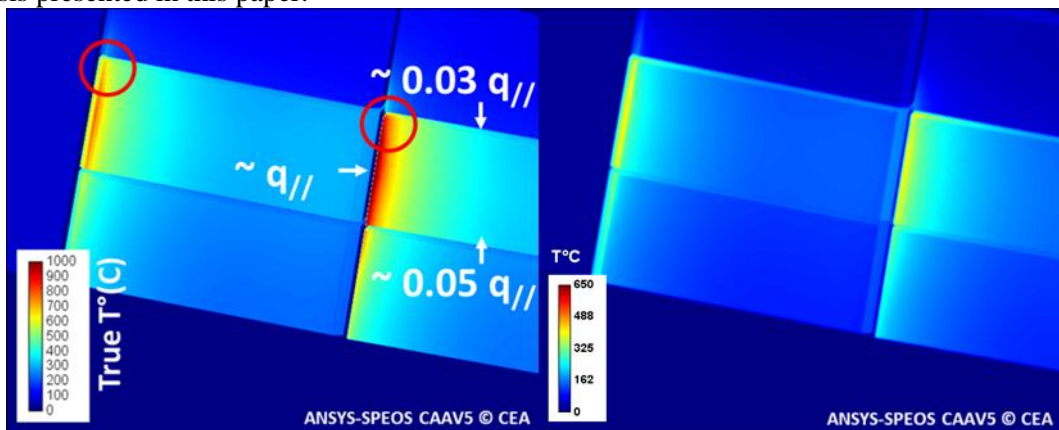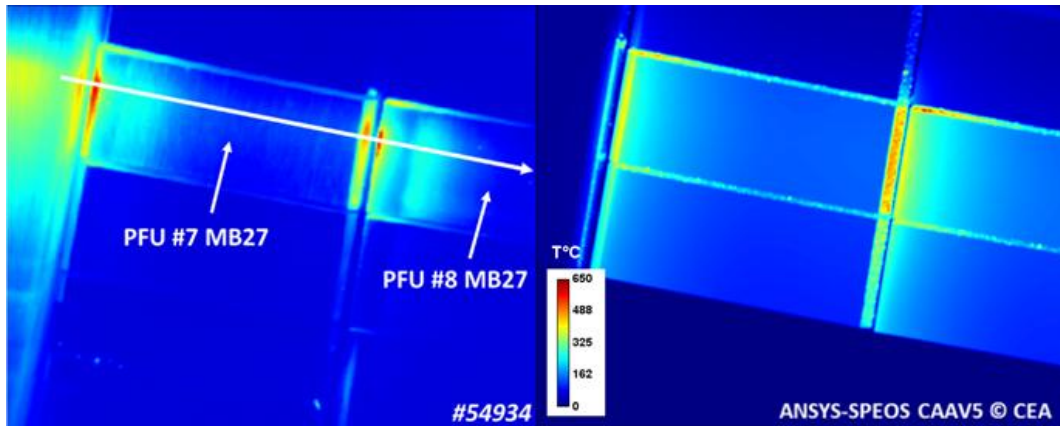
Figure 10 Three steps of the ANSYS-SPEOS simulations that give synthetic data based on OA modeling taking into account: the optical blurring (top left panel), the isotropic emissivity spatially uniform on surfaces (top right panel), and the complex model reflectance with Lambertian emission: 40% diffuse and 60% specular (bottom right panel), are compared to the VHR IR data (bottom left panel).

The slight temperature increase observed in the 3D FEM modeling (Figure 9) is not sufficient to appear in the synthetic data featuring the blurring of the optical system (left panel of Figure 10). When applying relevant emissivity on the surface observed in the FoV, based on measurements performed in Figure 6 at 50°C and extrapolated to the top LE corner temperature ~1200°C, it is possible to detect the hot spot on top LE corner, but still, not as important as it is in the VHR IR data. When the complex reflectance model is applied (bottom right panel of Figure 10), simulations clearly show a hot spot at the top LE corner as seen in VHR IR data (bottom left panel of Figure 10). It is also interesting to see that reflectance model highlights the reflections in the chamfered trailing edge of PFU #7 as observed in IR data. The analysis proposed here is a qualitative first step to illustrate how emissivity and reflections can affect the IR data in the specific case of the VHR. The hot spot appearing in the trailing edge of PFU #7 is partly imputed to reflection phenomena. Even though, this specific area is magnetically shadowed and no plasma heat flux is expected there, ions striking the LE are neutralized then can reflect from the surface and can carry power to the shadowed area. The relative importance of these phenomena have not been quantified in this work.

## 4.2. Temperature distribution based on IO modeling

The ion orbit model [25] considers the particle distribution around complex geometries such as the LEs and gaps. The helical trajectory, characterized by the Larmor radius, plays a significant role in the heat load distribution around poloidal and toroidal LEs. For ions, heavier than electrons, the size of the Larmor radius is typically ~0.35 mm during steady state L-mode in WEST, thus very close to the size of the gaps and misaligned LEs. For WEST, the incoming plasma is modelled as deuterium ions having a kinetic distribution of parallel speeds, and a Maxwellian distribution of perpendicular speeds. The electrons are treated under the optical approximation, because their Larmor radii are small enough to be ignored (~ μm size). Electric fields, which would arise in the magnetized Debye sheath near the surface, are not considered. Only the Larmor gyration of ions due to the Lorentz force is included. Several Larmor radii away from the surface, the ion velocities are assumed to be described by a collisionless kinetic presheath model [32], which predicts the ion distribution at the entrance of the sheath.

The ion orbit model predicts particle focusing onto the bottom LE corner (~4 times higher than at the top surface) due to Larmor radius trajectory of ions, despite it being magnetically shadowed. The angle of the VHR view of the divertor, implies that the bottom LE corner is hidden, while the top can be observed. One can imagine a reflection of the hot bottom LE corner in the toroidal gap and observed by the VHR system in the top LE corner. Heat flux simulation through IO modeling is performed in the top

panel of Figure 11. The thermal modeling with IOM heat flux distribution is displayed in the bottom panel of Figure 11.
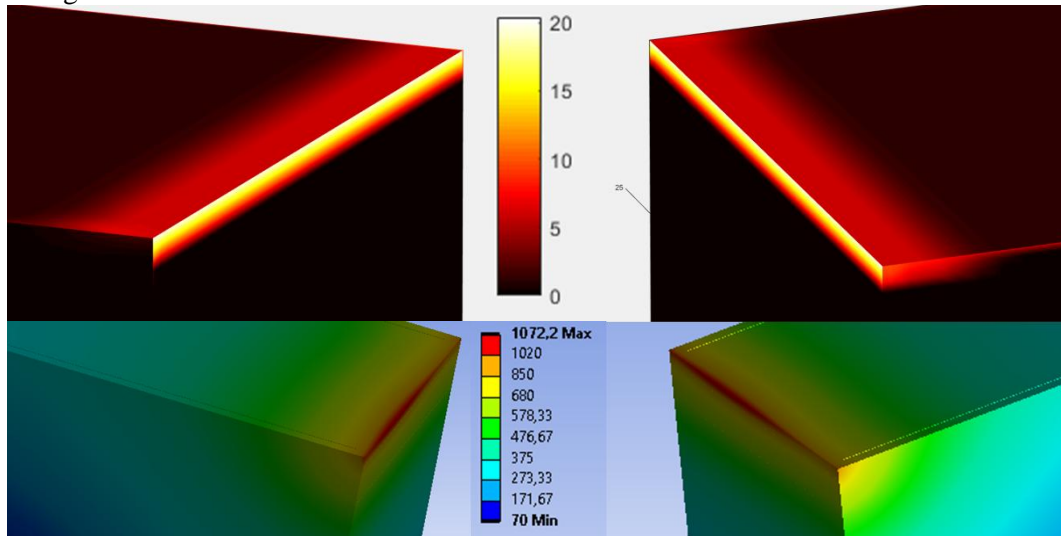


Figure 11 Top panel: normalized (1 MW.m$^{-2}$ on top surface far from the LE) 3D particle distribution using ion orbit modeling on a misaligned LE of PFU#8 MB27 (0.4 mm). The simulation considers the shadowing induced by the neighboring PFUs ([25]). Focus on the top LE corner in the toroidal gap between MB26 and MB27 (left), and bottom LE corner in the toroidal gap between MB27 and MB28 (right). Bottom panel: 3D FEM thermal modeling analogous to Figure 9, with IO modeling.

At the first sight, the temperature distribution pattern does not seem to be strongly affected by the ion Larmor radius effects. However slight discrepancies are observed from OA to IO modeling. For instance, the maximum temperature observed, which is slightly lower (1070°C) with the IO than with the OA modeling (1180°C). This is due to the ion Larmor smoothing effect observed at the poloidal LE, extensively studied numerically in [3]. At the top LE edge corner, where the hot spots appeared in the VHR IR data, there are no significant changes, where both evidence a slight increase of the temperature. A deeper look at the poloidal profiles of PFU #7 and #8 (Figure 12) confirms this observation.
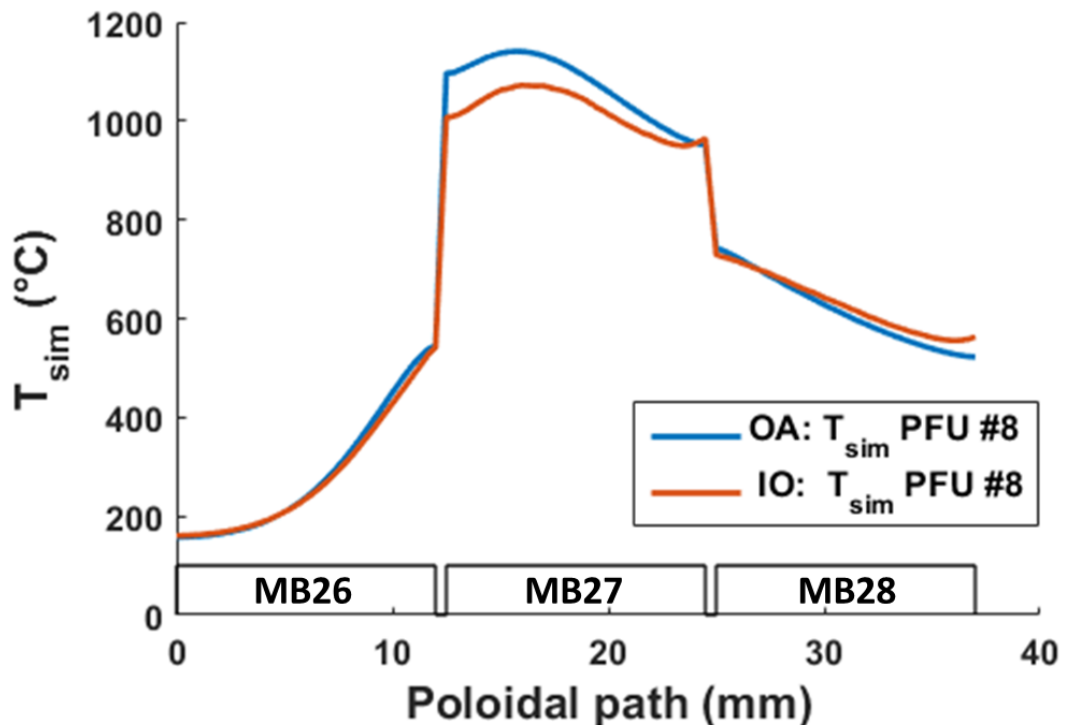
Figure 12 Poloidal profiles of the PFU #8 based on FGB measurements (71MW.m$^{-2}$, $\lambda_q$ = 18 mm and S = 5 mm), obtained through 3D FEM modeling based on OA (blue) and IO (red) heat flux modeling.

The main difference lies in the bottom LE corner, where the toroidal surface is not expected to be wetted with the OA modeling, while it should receive 4 times the heat flux received at the top surface with IO modeling. The question raised here is how that increase of temperature in the bottom LE corner affects the IR data at the top LE edge corner of the next MB. Analogous ANSYS-SPEOS simulations are performed to see the impact of the hot bottom LE corner, caused by the IO heat flux distribution, on synthetic temperature distribution.
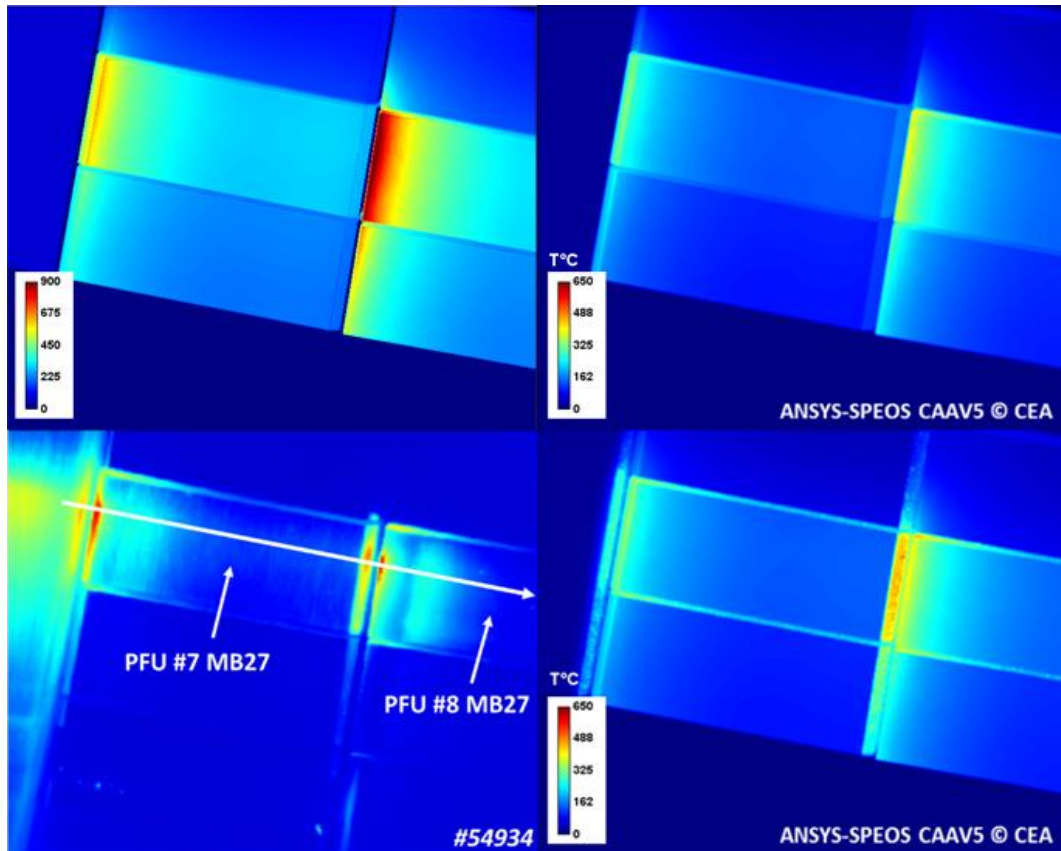
Figure 13 Three steps of the ANSYS-SPEOS simulations that give synthetic data base on IO modeling taking into account: the optical blurring (top left panel), the isotropic emissivity spatially uniform on surfaces (top right panel), and the complex model reflectance with Lambertian emission: 40% diffuse and 60% specular (bottom right panel), are compared to the VHR IR data (bottom left panel).

Similar pattern is observed with the IO modeling, the optical blurring is not sufficient to detect the hot spot in the top LE corner. The application of relevant emissivity in the different surfaces observed by the VHR shows a slight temperature increase in this specific area, even though the apparent temperatures are lower than the one measured in the poloidal LE. The use of a complex reflectance model highlights the temperature increase observed previously in the top LE corner with temperature similar to the one measured at the poloidal LE. One can note here that the lower toroidal edge has higher temperature than predicted by the thermal modeling. This effect is enhanced by the complex reflectance model around the toroidal gaps.

## 4. Conclusion

During the C4 experimental campaign in the WEST tokamak (2019), the use of a MWIR filter in the VHR IR system permitted to measure lower temperatures and study the full MB length, in the poloidal and toroidal directions. The analysis of the IR data showed an unexpected temperature drop in the toroidal profile, in the first 4 mm after the poloidal LE, but also the appearance of a hot spot in the top LE corner. A post-mortem emissivity measurement was performed after the C4 campaign in the PFUs monitored by the VHR IR camera. The emissivity measurement exhibits strong variation in the toroidal and poloidal directions. A drop of emissivity from 0.45 down to 0.15 is observed in the first 4 mm after the poloidal leading edge which is consistent with the temperature drop measured with the VHR IR system during the experiment. The emissivity drop reflects a more polished surface that may be attributed to the strong plasma wall interaction in this particular area. In the case of the toroidal leading

edge, the OA modeling does not predict any significant heat load here. Photonic simulations, using relevant parameters (distinct emissivity in top, poloidal and toroidal surfaces, realistic reflectance models and blurring effects of the optical system), showed that it is possible to observe significant hot spots in synthetic VHR IR data with only marginal heat load. The potential effect of the ion Larmor radius in the toroidal gaps was extensively investigated. With the inclination of the magnetic field on the OSP of the WEST divertor, the electrons and ions are supposed to wet two different sides of the MBs. With the maximum heat flux centered on the MB, thermal modeling using heat flux distribution given by the IO modeling does not show any significant changes at the HFS toroidal LE (exposed to electrons), compared to the OA modeling, while slight difference is observed in the LFS toroidal LE (exposed to ions). The main difference is observed at the poloidal LE, where the temperature is lower with IO due to the smoothing effect of ion Larmor radius at the poloidal LE. Thus, the temperature ratio between top LE corner and poloidal LE is reduced with the IO but not enough to explain the hot spot observed in the toroidal leading edge.

## Acknowledgement

## References

[1]  J. Bucalossi *et al.*, "The WEST project: Testing ITER divertor high heat flux component technology in a steady state tokamak environment," *Fusion Engineering and Design*, vol. 89, no. 7, pp. 907–912, Oct. 2014, doi: 10.1016/j.fusengdes.2014.01.062.

[2]  M. Missirlian, M. Firdaouss, M. Richou, P. Languille, S. Lecocq, and M. Lipa, "The WEST project: PFC shaping solutions investigated for the ITER-like W divertor," *Fusion Engineering and Design*, vol. 88, no. 9, pp. 1793–1797, Oct. 2013, doi: 10.1016/j.fusengdes.2013.03.048.

[3]  J. P. Gunn *et al.*, "Surface heat loads on the ITER divertor vertical targets," *Nucl. Fusion*, vol. 57, no. 4, p. 046025, 2017, doi: 10.1088/1741-4326/aa5e2a.

[4]  A. Grosjean *et al.*, "Very High-Resolution Infrared imagery of misaligned tungsten monoblock edge heating in the WEST tokamak," *Nuclear Materials and Energy*, p. 100910, Jan. 2021, doi: 10.1016/j.nme.2021.100910.

[5]  Y. Corre *et al.*, "Methodology for heat flux investigation on leading edges using infrared thermography," *Nucl. Fusion*, vol. 57, no. 1, Art. no. 1, Oct. 2016, doi: 10.1088/0029-5515/57/1/016009.

[6]  R. Dejarnac, J. P. Gunn, P. Vondracek, M. Komm, R. Panek, and R. A. Pitts, "Physics of toroidal gap heat loading on castellated plasma-facing components," *Nuclear Materials and Energy*, vol. 19, pp. 19–27, May 2019, doi: 10.1016/j.nme.2019.02.010.

[7]  J. W. Coenen *et al.*, "ELM-induced transient tungsten melting in the JET divertor," *Nucl. Fusion*, vol. 55, no. 2, Art. no. 2, Jan. 2015, doi: 10.1088/0029-5515/55/2/023010.

[8]  J. W. Coenen *et al.*, "ELM induced tungsten melting and its impact on tokamak operation," *Journal of Nuclear Materials*, vol. 463, pp. 78–84, Aug. 2015, doi: 10.1016/j.jnucmat.2014.08.062.

[9]  Y. Corre *et al.*, "Thermal analysis of protruding surfaces in the JET divertor," *Nucl. Fusion*, vol. 57, no. 6, Art. no. 6, Apr. 2017, doi: 10.1088/1741-4326/aa687e.

[10]  J. Gaspar *et al.*, "Heat flux analysis of Type-I ELM impact on a sloped, protruding surface in the JET bulk tungsten divertor," *Nuclear Materials and Energy*, vol. 17, pp. 182–187, Dec. 2018, doi: 10.1016/j.nme.2018.10.009.

[11]  K. Krieger *et al.*, "Investigation of transient melting of tungsten by ELMs in ASDEX Upgrade," *Phys. Scr.*, vol. T170, p. 014030, Oct. 2017, doi: 10.1088/1402-4896/aa8be8.

[12] J. W. Coenen *et al.*, "Tungsten melt layer motion and splashing on castellated tungsten surfaces at the tokamak TEXTOR," *Journal of Nuclear Materials*, vol. 415, no. 1, Supplement, Art. no. 1, Supplement, Aug. 2011, doi: 10.1016/j.jnucmat.2010.09.046.

[13] R. E. Nygren *et al.*, "Thermal management of tungsten leading edges in DIII-D," *Fusion Engineering and Design*, vol. 124, pp. 271–275, Nov. 2017, doi: 10.1016/j.fusengdes.2017.04.060.

[14] S. Hong *et al.*, "Inter-ELM heat loads on tungsten leading edge in the KSTAR divertor," *Nuclear Materials and Energy*, vol. 12, pp. 1122–1129, Aug. 2017, doi: 10.1016/j.nme.2017.02.005.

[15] T. W. Morgan, M. A. van den Berg, G. D. Temmerman, S. Bardin, D. U. B. Aussems, and R. A. Pitts, "Power deposition on misaligned castellated tungsten blocks in the Magnum-PSI and Pilot-PSI linear devices," *Nucl. Fusion*, vol. 57, no. 12, Art. no. 12, Sep. 2017, doi: 10.1088/1741-4326/aa8109.

[16] T. W. Morgan *et al.*, "A high-repetition rate edge localised mode replication system for the Magnum-PSI and Pilot-PSI linear devices," *Plasma Physics and Controlled Fusion*, vol. 56, no. 9, Art. no. 9, Sep. 2014, doi: 10.1088/0741-3335/56/9/095004.

[17] A. Grosjean *et al.*, "First analysis of the misaligned leading edges of ITER-like plasma facing units using a very high resolution infrared camera in WEST," *Nucl. Fusion*, vol. 60, no. 10, Art. no. 10, Oct. 2020, doi: 10.1088/1741-4326/ab9fa6.

[18] M. Diez *et al.*, "First evidence of optical hot spots on ITER-like plasma facing units in the WEST tokamak," *Nucl. Fusion*, Feb. 2020, doi: 10.1088/1741-4326/ab7891.

[19] J. Gaspar *et al.*, "Emissivity measurement of tungsten plasma facing components of the WEST tokamak," *Fusion Engineering and Design*, vol. 149, p. 111328, Dec. 2019, doi: 10.1016/j.fusengdes.2019.111328.

[20] J. Gaspar *et al.*, "In-situ assessment of the emissivity of tungsten plasma facing components of the WEST tokamak," *Nuclear Materials and Energy*, vol. 25, p. 100851, Dec. 2020, doi: 10.1016/j.nme.2020.100851.

[21] R. Dejarnac *et al.*, "Flush-mounted Langmuir probes in the WEST tokamak divertor," *Fusion Engineering and Design*, vol. 163, p. 112120, Feb. 2021, doi: 10.1016/j.fusengdes.2020.112120.

[22] M. Missirlian *et al.*, "The WEST project: Current status of the ITER-like tungsten divertor," *Fusion Engineering and Design*, vol. 89, no. 7, pp. 1048–1053, Oct. 2014, doi: 10.1016/j.fusengdes.2014.01.050.

[23] L. Delpech *et al.*, "Coupling properties of the LHCD launchers in the WEST experiments," *AIP Conference Proceedings*, vol. 2254, no. 1, p. 080004, Sep. 2020, doi: 10.1063/5.0013637.

[24] M. Houry *et al.*, "The very high spatial resolution infrared thermography on ITER-like tungsten monoblocks in WEST Tokamak," *Fusion Engineering and Design*, vol. 146, pp. 1104–1107, Sep. 2019, doi: 10.1016/j.fusengdes.2019.02.017.

[25] J. P. Gunn *et al.*, "Ion orbit modelling of ELM heat loads on ITER divertor vertical targets," *Nuclear Materials and Energy*, vol. 12, pp. 75–83, Aug. 2017, doi: 10.1016/j.nme.2016.10.005.

[26] M. Komm, J. P. Gunn, R. Dejarnac, R. Pánek, R. A. Pitts, and A. Podolník, "Particle-in-cell simulations of the plasma interaction with poloidal gaps in the ITER divertor outer vertical target," *Nucl. Fusion*, vol. 57, no. 12, Art. no. 12, Oct. 2017, doi: 10.1088/1741-4326/aa8a9a.

[27] A. Grosjean, "Impact de la géométrie et de l'alignement des cibles en tungstène sur la génération des points chauds dans WEST," These en préparation, Aix-Marseille, 2018.

[28] M.-H. Aumeunier *et al.*, "Infrared thermography in metallic environments of WEST and ASDEX Upgrade," *Nuclear Materials and Energy*, vol. 26, p. 100879, Mar. 2021, doi: 10.1016/j.nme.2020.100879.

[29] M. Firdaouss, T. Batal, J. Bucalossi, P. Languille, E. Nardon, and M. Richou, "Heat flux depositions on the WEST divertor and first wall components," *Fusion Engineering and Design*, vol. 98–99, pp. 1294–1298, Oct. 2015, doi: 10.1016/j.fusengdes.2014.12.024.

[30] "SPEOS Optical System Design Software | Ansys." https://www.ansys.com/products/optical/ansys-speos (accessed Nov. 28, 2020).

[31] M.-H. Aumeunier *et al.*, "Modeling of the ITER-like wide-angle infrared thermography view of JET," *Review of Scientific Instruments*, vol. 83, no. 10, p. 10D522, Jul. 2012, doi: 10.1063/1.4733532.

[32] K.-S. Chung and I. H. Hutchinson, "Kinetic theory of ion collection by probing objects in flowing strongly magnetized plasmas," *Phys. Rev. A*, vol. 38, no. 9, pp. 4721–4731, Nov. 1988, doi: 10.1103/PhysRevA.38.4721.